Jurnal Jamu Indonesia (2026) 11(4): 338–349
https://jamu-journal.ipb.ac.id/index.php/JJI/index

ISSN 2407-7178
eISSN 2407-7763

Research Article
Doi: https://doi.org/10.29244/jji.v11i4.476

Potential Active Compounds from Cashew (*Anacardium occidentale* L.) Leaves against SARS-CoV-2 RNA-Dependent RNA Polymerase: An *In Silico* Study

Senyawa Aktif Potensial dari Daun Jambu Mete (*Anacardium occidentale* L.) terhadap RNA-Dependent RNA Polymerase SARS-CoV-2: Studi *In Silico*

Willy Wijayanti[1], Nancy D. Yuliana[1], Endang Prangdimurti[1], Setyanto T. Wahyudi[2,3*]

[1]*Department of Food Science and Technology, Faculty of Engineering and Technology, IPB University, Bogor 16680, West Java, Indonesia*
[2]*Department of Physics, Faculty of Mathematics and Natural Sciences, IPB University, Bogor 16680, West Java, Indonesia*
[3]*Tropical Biopharmaca Research Center, IPB University, Taman Kencana Campus, Bogor 16128, West Java, Indonesia*

ARTICLE INFO

Article history
Received on: 2025-12-17
Revised on: 2026-01-10
Accepted on: 2026-07-17

Keyword:
Drug-likeness;
Molecular docking;
Molecular dynamics simulation;
Polyphenols;
SARS-CoV-2 RdRp

Kata kunci:
Kemiripan obat;
Penambatan molekuler;
Polifenol;
RdRp SARS-CoV-2;
Simulasi dinamika molekuler

ABSTRACT

Coronavirus disease 2019 (COVID-19), caused by Severe Acute Respiratory Syndrome Coronavirus 2 (SARS-CoV-2), has driven the search for effective antiviral candidates. SARS-CoV-2 RNA replication is catalyzed by RNA-dependent RNA polymerase (RdRp), making this enzyme a potential target for antiviral drug development. Cashew (*Anacardium occidentale* L.) leaves are traditionally consumed in Southeast Asia, and several of their polyphenolic compounds have been reported to inhibit RNA-dependent RNA polymerases of other RNA viruses. This study aimed to identify potential SARS-CoV-2 RdRp inhibitors through molecular docking and molecular dynamics simulations and to evaluate their drug-likeness and predicted bioactivity. Five polyphenolic compounds formed stable interactions with RdRp, as indicated by RMSD, RMSF, interaction energy, and radius of gyration analyses. These compounds warrant further *in vitro* and *in vivo* evaluation as candidate SARS-CoV-2 RdRp inhibitors.

ABSTRAK

Coronavirus disease 2019 (COVID-19), yang disebabkan oleh *Severe Acute Respiratory Syndrome Coronavirus* 2 (SARS-CoV-2), telah mendorong pencarian kandidat antivirus yang efektif. Replikasi RNA SARS-CoV-2 dikatalisis oleh RNA-dependent RNA polymerase (RdRp), sehingga enzim ini menjadi target potensial dalam pengembangan obat antivirus. Daun jambu mete (*Anacardium occidentale* L.) secara tradisional dikonsumsi di Asia Tenggara, dan beberapa senyawa polifenolnya dilaporkan mampu menghambat RNA-dependent RNA polymerase pada virus RNA lain. Penelitian ini bertujuan mengidentifikasi kandidat inhibitor RdRp SARS-CoV-2 melalui molecular docking dan simulasi dinamika molekuler serta mengevaluasi drug-likeness dan prediksi bioaktivitasnya. Lima senyawa polifenol menunjukkan interaksi yang stabil dengan RdRp berdasarkan analisis RMSD, RMSF, energi interaksi, dan jari-jari girasi. Senyawa tersebut perlu dievaluasi lebih lanjut melalui pengujian *in vitro* dan *in vivo* sebagai kandidat inhibitor RdRp SARS-CoV-2.

*Corresponding author:
Setyanto T. Wahyudi (stwahyudi@apps.ipb.ac.id)

© 2026 Authors. This is an open-access article distributed under the terms of the Creative Commons Attribution-NonCommercial-ShareAlike 4.0 International License (http://creativecommons.org/licenses/by-nc-sa/4.0/)

Citation: Wijayanti, W., Yuliana, N. D., Prangdimurti, E., & Wahyudi, S. T. (2026). Potential Active Compounds from Cashew (*Anacardium occidentale* L.) Leaves against SARS-CoV-2 RNA-Dependent RNA Polymerase: An *In Silico* Study. *Jurnal Jamu Indonesia*, *11*(4), 338–349. https://doi.org/10.29244/jji.v11i4.476

1. INTRODUCTION

The coronavirus disease 2019 (COVID-19) pandemic, caused by Severe Acute Respiratory Syndrome Coronavirus 2 (SARS-CoV-2), emerged as a major global health challenge (Porcheddu et al., 2020). The first reported cases were identified in Wuhan, China, in December 2019. By 20 June 2022, the World Health Organization (WHO) had recorded more than 535 million confirmed cases worldwide. Epidemiological evidence demonstrated rapid person-to-person transmission, which contributed to the difficulty of controlling the spread of SARS-CoV-2 (Chan et al., 2020; Chen et al., 2020).

SARS-CoV-2 belongs to the genus *Betacoronavirus* and is a positive-sense, single-stranded RNA virus. Its proteins can be broadly classified into structural proteins, including spike (S), nucleocapsid (N), membrane (M), and envelope (E) proteins, and non-structural proteins, including chymotrypsin-like protease (3CLpro), RNA-dependent RNA polymerase (RdRp), and papain-like protease (PLpro) (Cui, 2019). RdRp plays an essential role in viral RNA replication and is therefore an important molecular target for antiviral development. Its active site is accessible to small molecules, further supporting its potential as a target for SARS-CoV-2 inhibitor discovery (Elfiky, 2021).

Epigallocatechin gallate (EGCG), one of the major polyphenols in green tea, has been reported to exhibit antiviral activity, including inhibition of endonuclease activity in the influenza A virus RNA polymerase complex and disruption of viral replication through modulation of the cellular redox environment (Ho et al., 2009; Kuzuhara et al., 2009). *In silico* studies have also indicated that several plant-derived polyphenols can interact with SARS-CoV-2 RdRp and may interfere with viral RNA replication (Singh et al., 2021). Cashew (*Anacardium occidentale* L.) leaves are another source of polyphenolic compounds and are traditionally consumed or used in herbal preparations in several regions of Southeast Asia (Sae-leaw & Benjakul, 2018; Sinlapapanya et al., 2022). However, specific polyphenols from cashew leaves remain insufficiently explored as potential SARS-CoV-2 RdRp inhibitors. This gap supports further investigation of cashew leaf polyphenols as potential natural-product-derived antiviral candidates.

Conventional drug discovery is often time-consuming and resource-intensive, making computational approaches useful for the preliminary screening of bioactive compounds. *In silico* methods, particularly molecular docking and molecular dynamics simulations, can be used to predict ligand binding affinity, binding orientation, and the stability of protein-ligand complexes. Molecular docking provides an initial estimate of the interaction between candidate polyphenols and SARS-CoV-2 RdRp (Lyu et al., 2019), whereas molecular dynamics simulations provide further information on the stability and dynamic behavior of the resulting complexes (Shan et al., 2011). Accordingly, this study aimed to identify potential SARS-CoV-2 RdRp inhibitors from cashew leaf polyphenols using molecular docking and molecular dynamics simulations and to evaluate their drug-likeness and predicted bioactivity.

2. METHODS

2.1. Collection and Preparation of Candidate Compounds

A total of 30 compounds reported in cashew (*Anacardium occidentale* L.) leaves were compiled from the literature (**Table S1**). The three-dimensional structures of these compounds were downloaded from the PubChem database (National Center for Biotechnology Information, Bethesda, MD, USA; https://pubchem.ncbi.nlm.nih.gov/) in SDF format. The structures were converted from SDF to PDB format using UCSF Chimera version 1.14.0 (University of California, San Francisco, CA, USA) (Pettersen et al., 2004). Geometry optimization was subsequently performed using ORCA version 5.0.3 (FAccTs GmbH, Cologne, Germany) in combination with the def2-SVP basis set and Grimme's D3 dispersion correction (B3LYP-D3/def2-SVP). The optimized structures were then converted to PDBQT format using AutoDockTools version 1.5.6 (The Scripps Research Institute, La Jolla, CA, USA) for subsequent molecular docking.

2.2. Receptor Collection and Preparation

The three-dimensional structure of SARS-CoV-2 RNA-dependent RNA polymerase (RdRp) was obtained from the RCSB Protein Data Bank (https://www.rcsb.org/) using PDB ID 7BV2. This structure comprises the nsp12-nsp7-nsp8 polymerase complex bound to template-primer RNA and remdesivir triphosphate (RTP). The nsp12 subunit was used as the principal receptor for molecular docking.

2.3. Reference-Ligand Redocking

The RdRp receptor and the bound reference ligand were prepared using UCSF Chimera version 1.14.0 (University of California, San Francisco, CA, USA) (Pettersen et al., 2004). In the RdRp structure, only chain A and the co-crystallized ligand (ID F86) were selected for the redocking stage, while water molecules, other chains, and metal ions were removed from the RdRp structure. During the receptor preparation stage, hydrogen atoms were also added to the RdRp structure. Redocking of RTP to RdRp was performed using AutoDock Vina version 1.1.2 (The Scripps Research Institute, La Jolla, CA, USA) (Trott & Olson, 2010). The docking search space was centered at (x, y, z) = (91.788, 91.838, 104.806) Å with box dimensions of 20 × 20 × 20 Å and an exhaustiveness value of 16. Docking results were expressed as predicted binding energies (ΔG, kcal/mol).

2.4. Initial Screening using AutoDock Vina

The 30 prepared compounds were subjected to virtual screening against SARS-CoV-2 RdRp using AutoDock Vina version 1.1.2 (The Scripps Research Institute, La Jolla, CA, USA). The docking search space and parameters were based on those established during reference-ligand redocking. Three independent docking runs were performed for each compound to assess the consistency of the predicted binding results. Compounds were subsequently ranked according to their predicted binding energies, with more negative values representing more favorable predicted interactions within the docking model.

2.5. Pose Refinement using AutoDock4

The ten compounds with the most favorable predicted binding energies from the initial AutoDock Vina screening were subjected to pose refinement using AutoDock4 version 4.2.6 (The Scripps Research Institute, La Jolla, CA, USA) (Morris et al., 2009). During the docking stage, AutoDock4 was executed using the Lamarckian Genetic Algorithm (LGA) with 25,000,000 energy evaluations, a population size of 300, and 100 iterations (runs). The docking results yielded various positions (poses) that were clustered based on an RMSD tolerance of 2.0 Å. Subsequently, for each compound, the pose with the lowest binding energy from the dominant cluster was selected to represent the docking result. Three independent docking runs were performed for each ligand using grid-box dimensions of 23 × 23 × 23 Å and the ligand-specific grid-box center coordinates presented in **Table 1**. Docked complexes were visualized using PyMOL version 2.4.0 (Schrödinger, New York, NY, USA) and UCSF Chimera version 1.14.0 (University of California, San Francisco, CA, USA). Protein-ligand interactions were analyzed using LigPlot+ version 2.2.4 (European Bioinformatics Institute, Hinxton, UK) (Laskowski & Swindells, 2011). The five compounds with the most favorable mean predicted binding energies were selected for subsequent analyses.

2.6. Drug-Likeness, ADMET, and Predicted Bioactivity

The drug-likeness properties of the five compounds selected from AutoDock4 pose refinement were evaluated using the Drug-Likeness Tool (DruLiTo; National Institute of Pharmaceutical Education and Research, Mohali, India). Predicted bioactivity was evaluated using Molinspiration Cheminformatics (Molinspiration Cheminformatics, Bratislava, Slovakia; https://www.molinspiration.com). In addition, the pharmacokinetic properties and toxicity of the candidate compounds were predicted using the admetSAR 3.0 platform (East China University of Science and Technology, Shanghai, China; https://lmmd.ecust.edu.cn/admetsar3).

2.7. Molecular Dynamics System Preparation

The five highest-ranked complexes from AutoDock4 pose refinement, comprising agathisflavone, amentoflavone, quercetin 3′-xyloside, epicatechin-3-gallate, and peonidin, were selected as the starting structures for molecular dynamics (MD) simulations. Initial protein preparation was performed using the pdb4amber module in AmberTools20 (University of California, San Francisco, CA, USA) to identify structural gaps, add hydrogen atoms, and complete missing atoms where applicable. The protonation states of ionizable amino acid residues were determined using the H++ web server at pH 7. System parameterization was performed using the General AMBER force field (GAFF) (Wang et al., 2004) for the ligand and the AMBER force field 14SB (Maier et al., 2015) for the RdRp protein. The selected ligand was then processed using Antechamber within AMBER20 to determine atomic partial charges via the AM1-BCC method.

Each protein-ligand complex was solvated in a truncated octahedral box extending 14 Å from the solute and containing 39,241 TIP3P water molecules. The system was neutralized and adjusted to a NaCl concentration of 0.154 M. The topology and initial coordinate files required for MD simulations were generated using the LEaP module in AMBER20 (University of California, San Francisco, CA, USA).

2.8. Molecular Dynamics Simulation

Molecular dynamics simulations were conducted in four sequential stages: energy minimization, heating, equilibration, and production. All simulations were performed using AMBER20 (University of California, San Francisco, CA, USA). Energy minimization was conducted in five successive steps with progressively reduced positional restraints.

Table 1. Grid-box center coordinates used for AutoDock4 pose refinement

Compound	Center coordinates (x, y, z), Å
Amentoflavone	93.486, 89.756, 104.282
Epicatechin-3-gallate	93.362, 94.846, 103.904
Orientin-2″-O-gallate	94.655, 92.778, 105.705
Quercetin 3′-xyloside	90.568, 90.339, 106.831
Agathisflavone	91.860, 89.596, 106.548
Quercetin-4-O-glucoside	89.400, 89.613, 106.369
Quercetin 3-(2″-galloyl-α-L-arabinopyranoside)	92.296, 90.631, 104.553
Epigallocatechin-7-O-gallate	91.635, 91.153, 104.950
Peonidin	93.637, 95.436, 104.607
Quercetin-3-O-rutinoside	93.403, 90.024, 106.338

In the first step, harmonic restraints were applied to all protein atoms. In the second step, restraints were applied to all non-hydrogen protein atoms. In the third step, restraints were limited to the protein backbone atoms, whereas in the fourth step, only Cα atoms were restrained. A harmonic restraint constant of 10 kcal mol^{-1} $Å^{-2}$ was applied during each restrained minimization step. The fifth minimization step was performed without restraints. Energy minimization used a combination of steepest descent and conjugate gradient algorithms. The system was subsequently heated from 0 to 310 K for 0.6 ns under the NVT ensemble. Protein atoms were restrained using a force constant of 10 kcal mol^{-1} $Å^{-2}$, and temperature was controlled using a Langevin thermostat with gamma_ln = 1 ps^{-1}. Equilibration was then conducted in two sequential stages. First, NVT equilibration was performed for 50 ps with positional restraints applied only to the protein backbone atoms. Next, NPT equilibration was performed for 500 ps with an integration time step of 1 fs. Bonds involving hydrogen atoms were constrained using the SHAKE algorithm. Pressure was regulated using a Monte Carlo barostat, while the temperature was maintained at 310.15 K using a Langevin thermostat with a collision frequency (γ_ln) of 2 ps^{-1}. Production MD simulations were performed for 500 ns at 310 K under the NPT ensemble without positional restraints, using gamma_ln = 5 ps^{-1} and a nonbonded interaction cutoff of 9 Å. Production trajectories were subsequently analyzed using the cpptraj module in AMBER20.

2.9. Analysis of Structural Stability and Protein–Ligand Interaction

Root mean square deviation (RMSD), root mean square fluctuation (RMSF), radius of gyration (Rg), and protein-ligand interaction energy were analyzed for each simulation system. RMSD was calculated based on protein backbone atoms, using the first frame of the production trajectory as the reference structure. The RMSD at time (t) was calculated using the equation:

$$RMSD = \sqrt{\frac{\sum_{i=1}^{N} m_i \left\| \mathbf{r}_i(t) - \mathbf{r}_i^{ref} \right\|^2}{\sum_i^N m_i}}$$

Where N is the total number of atoms in the complex; m_i is the mass of the i-th atom; $\mathbf{r}_i(t)$ denotes the position of the i-th atom at time t; and $\mathbf{r}_i^{ref}$ represents the position of the i-th atom in the reference structure.

In addition to RMSD, RMSF was used to measure the average movement of each protein atom/residue relative to its average position during the simulation period (Roe & Cheatham, 2013). RMSF can be calculated using the following equation:

$$RMSF = \sqrt{\langle x_i - \langle x_i \rangle \rangle^2}$$

where x_i represents the position of the i-th atom or residue at a given time during the simulation, while $\langle x_i \rangle$ denotes the average position of that atom or residue throughout the simulation.

To evaluate the compactness of the protein structure during the simulation, the radius of gyration was calculated using the following equation:

$$R_g = \sqrt{\frac{1}{N}\sum_{i=1}^{N}(r_i - r_{cm})^2}$$

Where N is the number of atoms analyzed, r_i is the position of the i-th atom, and r_{cm} is the position of the system's center of mass.

Meanwhile, the protein-ligand interaction energy was calculated for each frame of the production trajectory based on the contributions of van der Waals and electrostatic interactions between the RdRp protein and each ligand.

3. RESULTS AND DISCUSSION

3.1. Docking Protocol Validation and Initial Compound Screening

Redocking of remdesivir triphosphate (RTP), the reference ligand in the SARS-CoV-2 RNA-dependent RNA polymerase (RdRp) structure, was performed to evaluate the ability of the docking protocol to reproduce the experimentally observed binding pose. The redocked RTP showed a root-mean-square deviation (RMSD) of 2.63 Å relative to the crystallographic pose. Although this value exceeds the commonly applied RMSD criterion of ≤2 Å, RMSD values within the range of 2–3 Å have also been considered acceptable for docking-pose reproduction (Trott & Olson, 2010; Ramírez & Caballero, 2018). Thus, the RMSD of 2.63 Å indicates acceptable, although not optimal, reproduction of the reference ligand pose. Redocking of RTP yielded a predicted binding energy of −7.4 kcal/mol, which was used as a reference for evaluating the docking protocol.

A total of 30 compounds reported in cashew (*Anacardium occidentale* L.) leaves were subjected to virtual screening against SARS-CoV-2 RdRp. Remdesivir monophosphate was included separately as a reference compound in the screening dataset. Most of the cashew-leaf compounds showed predicted binding energies equal to or more favorable than that of remdesivir monophosphate (−7.4 kcal/mol; **Table 2**). The ten compounds with the most favorable predicted binding energies were selected for subsequent pose refinement using AutoDock4. Within the AutoDock Vina scoring model, more negative predicted binding energies indicate more favorable ligand-receptor interactions (Lang et al., 2025). Amentoflavone showed the most favorable predicted binding energy (−10.5 kcal/mol), followed by epicatechin-3-gallate (−9.9 kcal/mol), orientin-2″-O-gallate (−9.4 kcal/mol), quercetin 3′-xyloside (−9.3 kcal/mol), and agathisflavone (−9.2 kcal/mol).

3.2. Pose Refinement using AutoDock4

To refine and independently reassess the binding poses obtained from the initial AutoDock Vina screening, the ten highest-ranked cashew leaf compounds were redocked against SARS-CoV-2 RdRp

using AutoDock4. Remdesivir triphosphate (RTP) was used as the reference ligand and showed a predicted binding energy of −5.11 kcal/mol. The ten test compounds showed mean predicted binding energies ranging from −7.43 to −4.37 kcal/mol (**Table 3**). Based on their ranking, five compounds with mean predicted binding energies of ≤ −6.34 kcal/mol were selected for further analysis: agathisflavone, amentoflavone, quercetin 3′-xyloside, epicatechin-3-gallate, and peonidin.

Table 2. Predicted binding energies of the screened compounds against SARS-CoV-2 RdRp using AutoDock Vina

Ligand	CID	Predicted binding energy, ΔG (kcal/mol)
Amentoflavone	5281600	−10.5
Epicatechin-3-gallate	65056	−9.9
Orientin-2″-O-gallate	44257967	−9.4
Quercetin 3′-xyloside	44259228	−9.3
Agathisflavone	5281599	−9.2
Quercetin-4-O-glucoside	5320844	−9.0
Quercetin 3-(2″-galloyl-α-L-arabinopyranoside)	44259256	−8.9
Epigallocatechin-7-O-gallate	44257113	−8.8
Peonidin	441773	−8.7
Quercetin-3-O-rutinoside	5280805	−8.7
Gallocatechin	65084	−8.6
Quercetin-3-O-rhamnoside	5280459	−8.6
Myricetin	5281672	−8.5
Chlorogenic acid	1794427	−8.5
Catechin	9064	−8.5
Quercetin-3-O-glucoside	5280804	−8.4
Kaempferol	5280863	−8.3
Epicatechin	72276	−8.3
Quercetin	5280343	−8.2
Quercetin-3-O-galactoside	5281643	−8.1
Kaempferol-3-O-glucoside	5282102	−8.1
Fisetin-8-C-glucoside	5281615	−8.0
Catechin-5-O-gallate	15689618	−8.0
Kaempferol-3-O-arabinofuranoside	5748554	−7.9
Hinokiflavone	5281627	−7.7
Remdesivir monophosphate	121310009	−7.4
Epifisetinidiol-4alpha-OI	12305024	−7.4
Anthocyanidin	145858	−6.6
2-Methylpentanoic acid	6950109	−4.3
Hexanamide	12332	−4.1
Butanamide	10927	−3.7

Table 3. Predicted binding energies of the ten highest-ranked ligands against SARS-CoV-2 RdRp using AutoDock4.2.6

Ligand	ΔG_1* (kcal/mol)	ΔG_2* (kcal/mol)	ΔG_3* (kcal/mol)	Mean ΔG (kcal/mol)
Agathisflavone	−7.40	−7.74	−6.92	−7.43
Amentoflavone	−6.94	−7.40	−6.18	−6.84
Quercetin 3′-xyloside	−6.00	−7.37	−6.40	−6.59
Epicatechin-3-gallate	−5.98	−7.83	−5.48	−6.43
Peonidin	−6.47	−6.70	−5.85	−6.34
Quercetin 3-(2″-galloyl-α-L-arabinopyranoside)	−6.01	−6.23	−6.22	−6.15
Epigallocatechin-7-O-gallate	−5.73	−6.53	−6.04	−6.10
Quercetin-4-O-glucoside	−5.31	−5.86	−4.95	−5.37
Quercetin-3-O-rutinoside	−5.08	−5.80	−4.05	−4.98
Orientin-2″-O-gallate	−4.73	−5.00	−3.37	−4.37

*All docking runs used the same grid-box dimensions (23 × 23 × 23 Å), with ligand-specific center coordinates listed in **Table 1**.

The predicted binding poses of the five selected compounds within the SARS-CoV-2 RdRp binding region are shown in **Figure 1**. Their corresponding two-dimensional interaction profiles are presented in **Figure 2** and summarized in **Table 4**. Each compound exhibited a distinct pattern of hydrogen bonding and hydrophobic contacts with residues surrounding the binding region.

Agathisflavone formed a hydrogen bond with Asp760 and hydrophobic contacts with Cys622, Arg555, and Arg836. Amentoflavone formed hydrogen bonds with Arg555, Arg553, Ser759, Asn691, and Ser682 and hydrophobic contacts with Lys545, Ala688, Asp760, Thr687, and Asp623. Quercetin 3′-xyloside formed hydrogen bonds with Arg836, Ile548, and Ser682 and hydrophobic contacts with Ala547, Arg555, and Thr687. Epicatechin-3-gallate formed hydrogen bonds with Asp760, Asn691, Cys622, Thr556, Tyr456, Arg624, and Ser682 and hydrophobic contacts with Asp623, Thr680, and Ser681. Peonidin formed hydrogen bonds with Asp760, Ser759, Arg555, Thr556, Arg624, Tyr456, and Asp452 and hydrophobic contacts with Asp623, Ser682, Ser681, Thr687, Ala688, and Asn691.

Several residues involved in the interactions of the selected compounds, particularly Arg555, Ser759, Asp760, and Ser682, are located within or near functionally important regions of SARS-CoV-2 RdRp. Residues 759–761, together with Lys545 and Arg555, have been associated with RNA synthesis and ligand recognition within the polymerase complex (Yin et al., 2020). Other residues, including Ser759, Asp760, Asp761, Asp618, and Ser682, have also been reported within the functional region of RdRp (Shannon et al., 2020). The interaction profile of the reference ligand RTP is shown separately in **Figure 3**. Comparison with the RTP interaction profile indicates that several selected compounds interact with residues located within the same functionally relevant region of RdRp. However, overlap in residue contacts alone does not establish an identical binding mode or equivalent inhibitory activity to RTP.

Table 4. Amino acid residues involved in interactions between the selected ligands and SARS-CoV-2 RdRp

Ligand	Hydrogen-bond interactions	Hydrophobic contacts
Agathisflavone	Asp760	Cys622, Arg555, Arg836
Amentoflavone	Arg555, Arg553, Ser759, Asn691, Ser682	Lys545, Ala688, Asp760, Thr687, Asp623
Quercetin 3′-xyloside	Arg836, Ile548, Ser682	Ala547, Arg555, Thr687
Epicatechin-3-gallate	Asp760, Asn691, Cys622, Thr556, Tyr456, Arg624, Ser682	Asp623, Thr680, Ser681
Peonidin	Asp760, Ser759, Arg555, Thr556, Arg624, Tyr456, Asp452	Asp623, Ser682, Ser681, Thr687, Ala688, Asn691

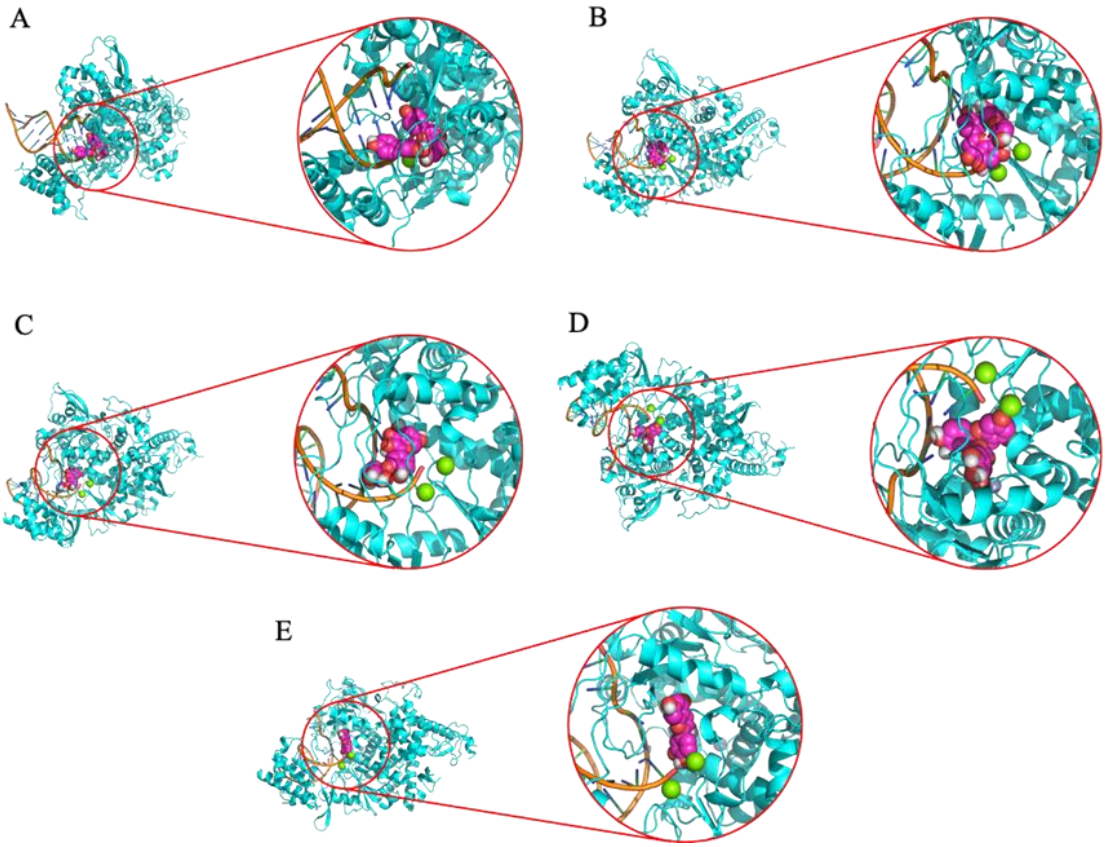


Figure 1. Predicted binding poses of the five selected compounds in the SARS-CoV-2 RdRp binding region: (A) agathisflavone, (B) amentoflavone, (C) quercetin 3′-xyloside, (D) epicatechin-3-gallate, and (E) peonidin. Insets show enlarged views of the predicted ligand-binding regions.

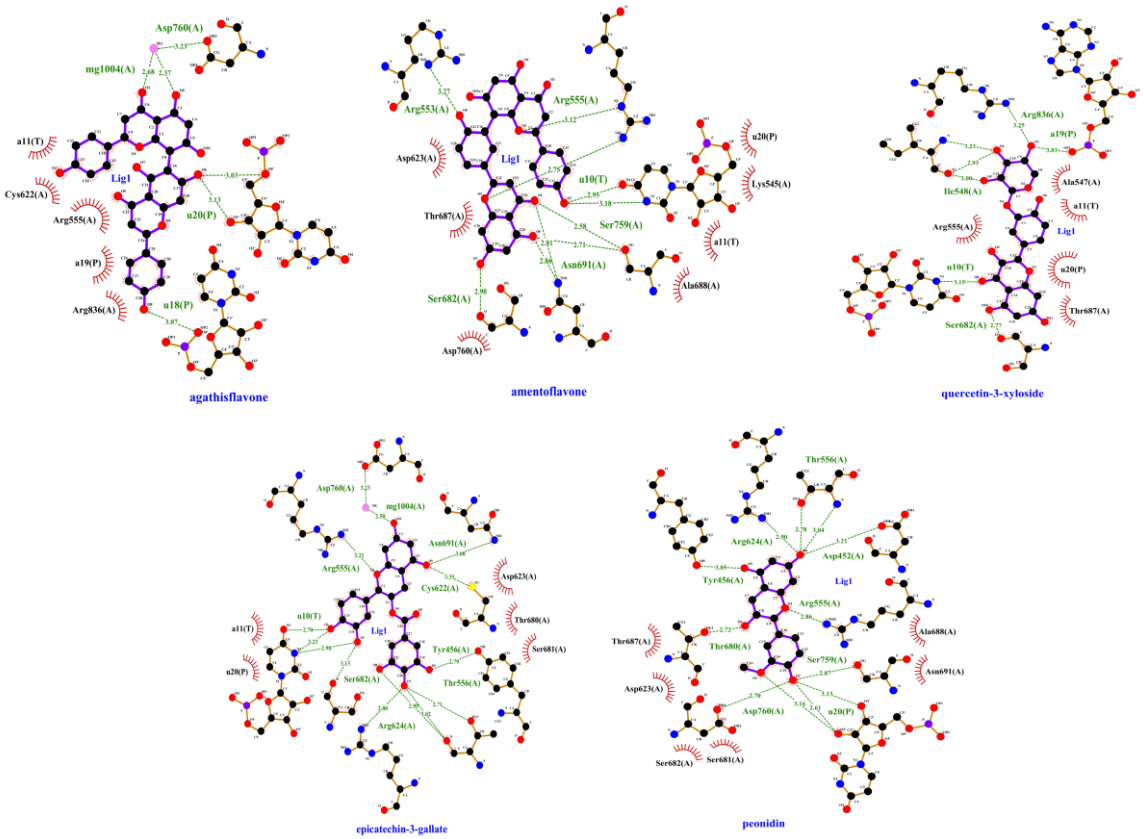


Figure 2. Two-dimensional interaction diagrams of the five selected compounds with SARS-CoV-2 RdRp: agathisflavone, amentoflavone, quercetin 3′-xyloside, epicatechin-3-gallate, and peonidin. Green dashed lines indicate hydrogen bonds, whereas red spoked arcs indicate hydrophobic contacts.

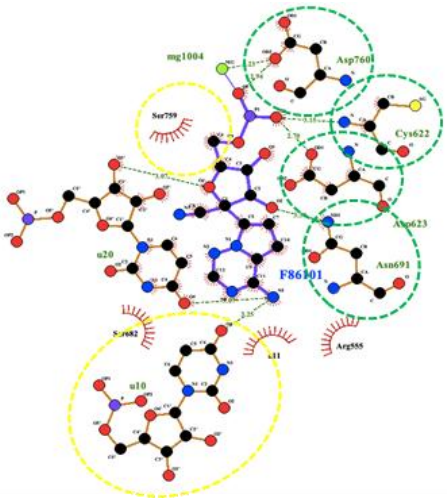


Figure 3. Two-dimensional interaction diagram of remdesivir triphosphate (RTP) with SARS-CoV-2 RdRp residues.

3.3. Drug-Likeness, Predicted Bioactivity, and ADMET Properties

The drug-likeness properties and predicted enzyme-inhibitor bioactivity scores of the five selected compounds are presented in **Table 5**. Peonidin satisfied all evaluated Lipinski and Veber criteria, with a molecular weight of 301.07 Da, log P of 1.86, five hydrogen-bond acceptors, four hydrogen-bond donors, a topological polar surface area (TPSA) of 90.15 Å^2, and two rotatable bonds. In contrast, agathisflavone and amentoflavone exceeded the recommended limits for molecular weight, hydrogen-bond donors, and TPSA. Quercetin 3′-xyloside exceeded the limits for hydrogen-bond acceptors, hydrogen-bond donors, and TPSA, whereas epicatechin-3-gallate exceeded the limits for hydrogen-bond donors and TPSA. Thus, peonidin was the only compound that met all of the evaluated drug-likeness criteria, while the other four compounds showed one or more rule violations.

The predicted enzyme-inhibitor (EI) scores ranged from −0.04 to 0.42. Quercetin 3′-xyloside showed the highest EI score (0.42), followed by epicatechin-3-gallate (0.25), amentoflavone (0.10), agathisflavone (0.06), and peonidin (−0.04). These values represent computational bioactivity scores and should therefore be interpreted as relative predictions of enzyme-inhibitor propensity

rather than evidence of experimentally demonstrated enzyme inhibition.

Predicted ADMET-related properties of the five selected compounds are presented in **Table 6**. The numerical predictions varied among compounds for blood-brain barrier (BBB) penetration, human intestinal absorption (HIA), AMES toxicity, and rat acute toxicity. Epicatechin-3-gallate and peonidin showed the highest BBB prediction values, whereas peonidin showed the highest HIA value among the five compounds. The predicted AMES toxicity values ranged from 0.142 to 0.560, while the predicted rat acute toxicity (LD_{50}) values ranged from 2.593 to 3.505 mol/kg. Because these parameters were obtained computationally, they should be regarded as preliminary screening indicators rather than direct evidence of absorption, brain penetration, mutagenicity, or *in vivo* safety. Accordingly, the ADMET predictions complement the molecular docking and drug-likeness analyses but do not independently establish the suitability of these compounds as drug candidates.

3.4. Molecular dynamics (MD) simulations

Molecular dynamics simulations were performed for 500 ns to evaluate the conformational behavior and stability of the five selected SARS-CoV-2 RdRp-ligand complexes. The simulation trajectories were analyzed using root-mean-square deviation (RMSD), root-mean-square fluctuation (RMSF), protein-ligand interaction energy, and radius of gyration (Rg). RMSD was used to assess conformational deviation from the initial structure over the course of the simulation (Edache et al., 2023). Agathisflavone, amentoflavone, quercetin 3′-xyloside, and epicatechin-3-gallate showed relatively stable RMSD profiles after approximately the first 20 ns, with values remaining close to 2 Å for most of the simulation (**Figure 4A**). The peonidin complex also maintained an RMSD of approximately 2 Å during the first 400 ns, followed by a gradual increase to approximately 2.7–3.0 Å toward the end of the simulation. Overall, the relatively stable RMSD profiles indicate limited conformational deviation in most complexes, whereas the late increase observed for peonidin suggests greater conformational variation during the final phase of the simulation.

RMSF analysis was used to evaluate residue-level flexibility during the simulations (Singh et al., 2021). Most residues showed fluctuations below 2 Å across the five complexes, indicating generally limited local flexibility (**Figure 4B**). The peonidin complex exhibited comparatively higher fluctuations in the approximately 240–300 residue region, suggesting increased local dynamics in this part of the protein. The protein-ligand interaction-energy profiles also remained relatively stable throughout the simulations (**Figure 4C**). The reported interaction-energy values were −92.59 kcal/mol for agathisflavone, −90.81 kcal/mol for amentoflavone, −84.85 kcal/mol for quercetin 3′-xyloside, −105.10 kcal/mol for epicatechin-3-gallate, and −56.43 kcal/mol for peonidin. Within the interaction-energy metric used in this study, more negative values indicate more favorable energetic interactions. Epicatechin-3-gallate showed the most negative interaction energy among the five complexes, whereas peonidin showed the least negative value.

The radius of gyration was analyzed to assess the overall compactness of the protein-ligand complexes during the simulations (Ojo et al., 2024). Rg values remained within a narrow range of approximately 28.64–28.84 Å throughout the 500 ns simulation (**Figure 4D**), indicating that the overall structural compactness of RdRp was largely maintained. Taken together, the RMSD, RMSF, interaction-energy, and Rg analyses indicate that the selected ligands formed computationally stable complexes with SARS-CoV-2 RdRp over most of the simulation period. However, the greater late-stage RMSD deviation and less favorable interaction energy observed for peonidin suggest comparatively greater conformational variability than that observed for the other selected complexes.

These computational findings are relevant because RdRp is essential for coronavirus RNA synthesis and represents an established molecular target for antiviral development (Elfiky, 2021; Subissi et al., 2014). Structural studies of SARS-CoV-2 RdRp and remdesivir further support the therapeutic relevance of this enzyme (Shannon et al., 2020; Yin et al., 2020). Nevertheless, the molecular dynamics results presented here describe predicted structural and energetic behavior and should not be interpreted as direct evidence of RdRp inhibition.

Polyphenols contain aromatic rings and hydroxyl groups that can support multiple non-covalent interactions with proteins, including hydrogen bonding, π–π interactions, and hydrophobic contacts (Panche et al., 2016). Previous studies have also reported antiviral activities of polyphenolic compounds against RNA viruses through several proposed mechanisms, including interference with viral replication processes (Lin et al., 2014).

Table 5. Drug-likeness properties and predicted enzyme-inhibitor bioactivity scores of the selected compounds

Ligand	MW (Da)	log P	HBA	HBD	TPSA (Å²)	nRB	EI
Agathisflavone	538.09	2.03	10	6	173.98	3	0.06
Amentoflavone	538.09	2.03	10	6	173.98	3	0.10
Quercetin 3′-xyloside	434.08	0.34	11	7	186.37	3	0.42
Epicatechin-3-gallate	442.09	2.64	10	7	177.14	4	0.25
Peonidin	301.07	1.86	5	4	90.15	2	−0.04

MW, molecular weight (≤500 Da); log P (≤5); HBA, hydrogen-bond acceptors (≤10); HBD, hydrogen-bond donors (≤5); TPSA, topological polar surface area (≤140 Å²); nRB, number of rotatable bonds (≤10); EI, predicted enzyme-inhibitor bioactivity score.

Table 6. Prediction of pharmacokinetic properties and toxicity of candidate compounds using admetSAR.

Compound	BBB	HIA	AMES toxicity	Rat acute toxicity, LD_{50} (mol/kg)
Agathisflavone	0.385	0.430	0.388	3.489
Amentoflavone	0.352	0.430	0.388	3.505
Quercetin 3′-xyloside	0.108	0.229	0.430	2.958
Epicatechin-3-gallate	0.861	0.328	0.560	2.915
Peonidin	0.746	0.449	0.142	2.593

BBB, blood-brain barrier; HIA, human intestinal absorption; AMES, bacterial reverse-mutation test; LD_{50}, median lethal dose.

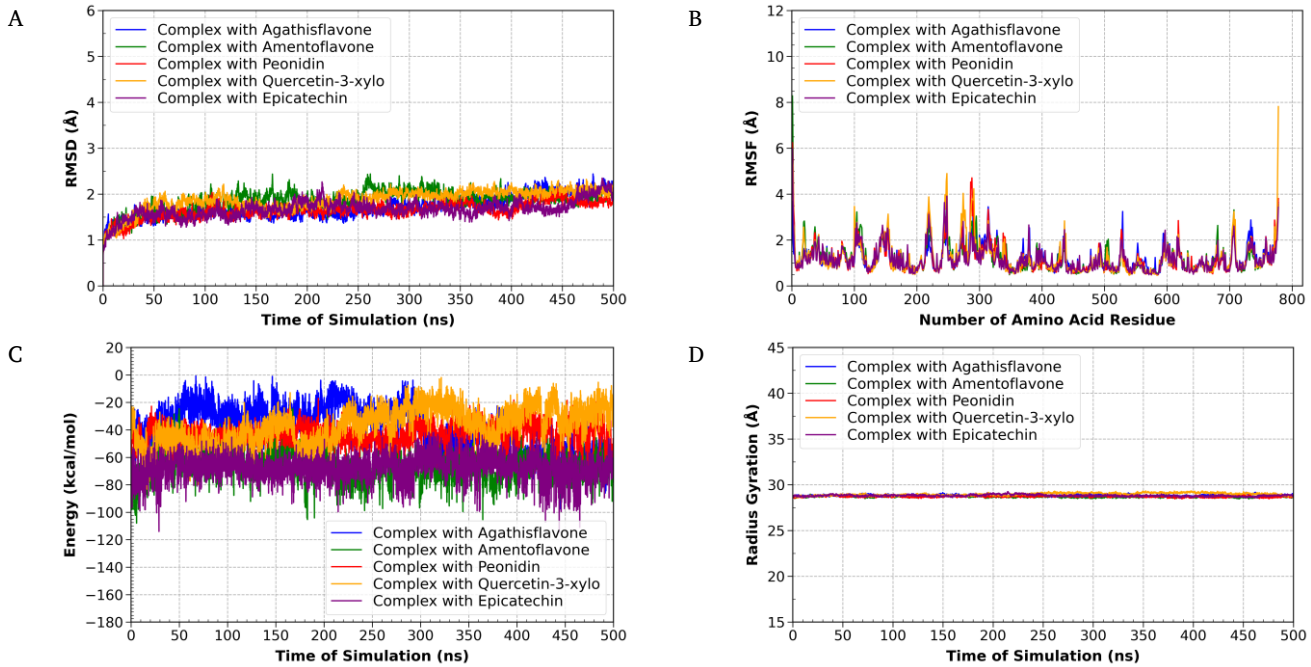


Figure 4. Molecular dynamics analyses of the five selected SARS-CoV-2 RdRp-ligand complexes over 500 ns: (A) root-mean-square deviation (RMSD, Å), (B) root-mean-square fluctuation (RMSF, Å), (C) protein-ligand interaction energy (kcal/mol), and (D) radius of gyration (Rg, Å).

In the present study, the generally stable conformational profiles, maintained structural compactness, and favorable interaction-energy profiles observed for several selected compounds support their further investigation as potential SARS-CoV-2 RdRp-binding candidates. These *in silico* findings require experimental validation through *in vitro* and, where appropriate, *in vivo* studies before antiviral activity or therapeutic potential can be established.

4. CONCLUSION

This *in silico* study identified five cashew leaf polyphenols as potential SARS-CoV-2 RNA-dependent RNA polymerase (RdRp) inhibitors. Among the 30 compounds screened using AutoDock Vina, agathisflavone, amentoflavone, quercetin 3′-xyloside, epicatechin-3-gallate, and peonidin were selected through sequential docking with AutoDock Vina and AutoDock4 and were further evaluated for drug-likeness, predicted bioactivity, and molecular dynamics behavior. Molecular dynamics simulations indicated generally stable conformational and interaction profiles for the selected RdRp-ligand complexes, although peonidin showed comparatively greater conformational variation during the later stage of the simulation. These computational findings support further *in vitro* and, where appropriate, *in vivo* validation of the selected compounds before their inhibitory activity against SARS-CoV-2 RdRp can be established.

AUTHOR CONTRIBUTIONS

Conceptualization, NDY and EP; methodology, STW; formal analysis, WW, NDY, and STW; investigation, WW; writing-original draft preparation, WW; writing-review and editing, NDY, EP, and STW. All authors have read and agreed to the published version of the manuscript.

INSTITUTIONAL REVIEW BOARD STATEMENT

Not applicable.

INFORMED CONSENT STATEMENT

Not applicable.

DATA AVAILABILITY STATEMENT

Data supporting the findings of this study are available upon reasonable request from the corresponding author.

FUNDING

This research received no external funding.

ACKNOWLEDGMENT

The authors acknowledge the computational resources provided by the HPC Lab, Theoretical Physics Division, Department of Physics, IPB University.

CONFLICTS OF INTEREST

The authors declare no conflict of interest.

ROLE OF FUNDERS

Not applicable because this research received no external funding.

DECLARATION OF GENERATIVE ARTIFICIAL INTELLIGENCE (AI) USE

During the preparation of this manuscript, the authors used ChatGPT (OpenAI) to assist in improving the clarity, structure, or readability of the text. After using this tool, the authors thoroughly reviewed, edited, and verified the entire content to ensure it accurately represents their own ideas and interpretations. The authors take full responsibility for the integrity and originality of the published work.

REFERENCES

Chan, J. F.-W., Yuan, S., Kok, K.-H., To, K. K.-W., Chu, H., Yang, J., Xing, F., Liu, J., Yip, C. C.-Y., Poon, R. W.-S., Tsoi, H.-W., Lo, S. K.-F., Chan, K.-H., Poon, V. K.-M., Chan, W.-M., Ip, J. D., Cai, J.-P., Cheng, V. C.-C., Chen, H., … Yuen, K.-Y. (2020). A familial cluster of pneumonia associated with the 2019 novel coronavirus indicating person-to-person transmission: A study of a family cluster. *The Lancet, 395*(10223), 514–523. https://doi.org/10.1016/S0140-6736(20)30154-9

Chen, N., Zhou, M., Dong, X., Qu, J., Gong, F., Han, Y., Qiu, Y., Wang, J., Liu, Y., Wei, Y., Xia, J., Yu, T., Zhang, X., & Zhang, L. (2020). Epidemiological and clinical characteristics of 99 cases of 2019 novel coronavirus pneumonia in Wuhan, China: A descriptive study. *The Lancet, 395*(10223), 507–513. https://doi.org/10.1016/S0140-6736(20)30211-7

Cui, J., Li, F., & Shi, Z.-L. (2019). Origin and evolution of pathogenic coronaviruses. *Nature Reviews Microbiology, 17*(3), 181–192. https://doi.org/10.1038/s41579-018-0118-9

Edache, E. I., Uzairu, A., Mamza, P. A., Shallangwa, G. A., Yagin, F. H., Abdel Samee, N., & Mahmoud, N. F. (2023). Combining docking, molecular dynamics simulations, AD-MET pharmacokinetics properties, and MMGBSA calculations to create specialized protocols for running effective virtual screening campaigns on the autoimmune disorder and SARS-CoV-2 main protease. *Frontiers in Molecular Biosciences, 10*, 1254230. https://doi.org/10.3389/fmolb.2023.1254230

Elfiky, A. A. (2021). SARS-CoV-2 RNA dependent RNA polymerase (RdRp) targeting: An *in silico* perspective. *Journal of Biomolecular Structure and Dynamics, 39*(9), 3204–3212. https://doi.org/10.1080/07391102.2020.1761882

Ho, H.-Y., Cheng, M.-L., Weng, S.-F., Leu, Y.-L., & Chiu, D. T.-Y. (2009). Antiviral effect of epigallocatechin gallate on enterovirus 71. *Journal of Agricultural and Food Chemistry, 57*(14), 6140–6147. https://doi.org/10.1021/jf901128u

Kuzuhara, T., Iwai, Y., Takahashi, H., Hatakeyama, D., & Echigo, N. (2009). Green tea catechins inhibit the endonuclease activity of influenza A virus RNA polymerase. *PLoS Currents, 1*, RRN1052. https://doi.org/10.1371/currents.RRN1052

Lang, S., Braz, N. F., Slater, M. J., & Kidley, N. J. (2025). *In silico* methods for ranking ligand–protein interactions and predicting binding affinities: Which method is right for you? *Journal of Medicinal Chemistry, 68*(19), 19795–19799. https://doi.org/10.1021/acs.jmedchem.5c02582

Laskowski, R. A., & Swindells, M. B. (2011). LigPlot+: Multiple ligand-protein interaction diagrams for drug discovery. *Journal of Chemical Information and Modeling, 51*(10), 2778–2786. https://doi.org/10.1021/ci200227u

Lin, L.-T., Hsu, W.-C., & Lin, C.-C. (2014). Antiviral natural products and herbal medicines. *Journal of Traditional and Complementary Medicine, 4*(1), 24–35. https://doi.org/10.4103/2225-4110.124335

Lyu, J., Wang, S., Balius, T. E., Singh, I., Levit, A., Moroz, Y. S., O'Meara, M. J., Che, T., Algaa, E., Tolmachova, K., Tolmachev, A. A., Shoichet, B. K., Roth, B. L., & Irwin, J. J. (2019). Ultra-large library docking for discovering new chemotypes. *Nature, 566*(7743), 224–229. https://doi.org/10.1038/s41586-019-0917-9

Maier, J. A., Martinez, C., Kasavajhala, K., Wickstrom, L., Hauser, K. E., & Simmerling, C. (2015). ff14SB: improving the accuracy of protein side chain and backbone parameters from ff99SB. *Journal of Chemical Theory and Computation*, *11*(8), 3696. https://doi.org/10.1021/acs.jctc.5b00255

Morris, G. M., Huey, R., Lindstrom, W., Sanner, M. F., Belew, R. K., Goodsell, D. S., & Olson, A. J. (2009). AutoDock4 and AutoDockTools4: Automated docking with selective receptor flexibility. *Journal of Computational Chemistry, 30*(16), 2785–2791. https://doi.org/10.1002/jcc.21256

Ojo, O. A., Ajayi-Odoko, O. A., Gyebi, G. A., Ayokunle, D. I., Ogunlakin, A. D., Ezenabor, E. H., Olanrewaju, A. A., Agbeye, O. D., Ogunwale, E. T., Rotimi, D. E., Fouad, D., Batiha, G. E.-S., & Adeyemi, O. S. (2024). Network pharmacology, molecular dynamics and *in vitro* assessments of indigenous herbal formulations for Alzheimer's therapy. *Life, 14*(10), 1222. https://doi.org/10.3390/life14101222

Panche, A. N., Diwan, A. D., & Chandra, S. R. (2016). Flavonoids: An overview. *Journal of Nutritional Science, 5*, e47. https://doi.org/10.1017/jns.2016.41

Pettersen, E. F., Goddard, T. D., Huang, C. C., Couch, G. S., Greenblatt, D. M., Meng, E. C., & Ferrin, T. E. (2004). UCSF Chimera: A visualization system for exploratory research and analysis. *Journal of Computational Chemistry, 25*(13), 1605–1612. https://doi.org/10.1002/jcc.20084

Porcheddu, R., Serra, C., Kelvin, D., Kelvin, N., & Rubino, S. (2020). Similarity in case fatality rates (CFR) of COVID-19/SARS-CoV-2 in Italy and China. *The Journal of Infection in Developing Countries, 14*(2), 125–128. https://doi.org/10.3855/jidc.12600

Ramírez, D., & Caballero, J. (2018). Is it reliable to take the molecular docking top scoring position as the best solution without considering available structural data? *Molecules, 23*(5), 1038. https://doi.org/10.3390/molecules23051038

Roe, D. R., & Cheatham III, T. E. (2013). PTRAJ and CPPTRAJ: software for processing and analysis of molecular dynamics trajectory data. *Journal of Chemical Theory and Computation*, *9*(7), 3084-3095. https://doi.org/10.1021/ct400341p

Sae-leaw, T., & Benjakul, S. (2019). Prevention of quality loss and melanosis of Pacific white shrimp by cashew leaf extracts. *Food Control, 95*, 257–266. https://doi.org/10.1016/j.foodcont.2018.08.014

Shan, Y., Kim, E. T., Eastwood, M. P., Dror, R. O., Seeliger, M. A., & Shaw, D. E. (2011). How does a drug molecule find its target binding site? *Journal of the American Chemical Society, 133*(24), 9181–9183. https://doi.org/10.1021/ja202726y

Shannon, A., Le, N. T.-T., Selisko, B., Eydoux, C., Alvarez, K., Guillemot, J.-C., Decroly, E., Peersen, O., Ferron, F., & Canard, B. (2020). Remdesivir and SARS-CoV-2: Structural requirements at both nsp12 RdRp and nsp14 exonuclease active-sites. *Antiviral Research, 178*, 104793. https://doi.org/10.1016/j.antiviral.2020.104793

Singh, S., Sk, M. F., Sonawane, A., Kar, P., & Sadhukhan, S. (2021). Plant-derived natural polyphenols as potential antiviral drugs against SARS-CoV-2 via RNA-dependent RNA polymerase (RdRp) inhibition: An *in silico* analysis. *Journal of Biomolecular Structure and Dynamics, 39*(16), 6249–6264. https://doi.org/10.1080/07391102.2020.1796810

Sinlapapanya, P., Sumpavapol, P., Nirmal, N., Zhang, B., Hong, H., & Benjakul, S. (2022). Ethanolic cashew leaf extract: Antimicrobial activity, mode of action, and retardation of spoilage bacteria in refrigerated Nile tilapia slices. *Foods, 11*(21), 3461. https://doi.org/10.3390/foods11213461

Subissi, L., Posthuma, C. C., Collet, A., Zevenhoven-Dobbe, J. C., Gorbalenya, A. E., Decroly, E., Snijder, E. J., Canard, B., & Imbert, I. (2014). One severe acute respiratory syndrome coronavirus protein complex integrates processive RNA polymerase and exonuclease activities. *Proceedings of the National Academy of Sciences of the United States of America, 111*(37), E3900–E3909. https://doi.org/10.1073/pnas.1323705111

Wang, J., Wolf, R. M., Caldwell, J. W., Kollman, P. A., & Case, D. A. (2004). Development and testing of a general amber force field. *Journal of Computational Chemistry*, *25*(9), 1157-1174.

Trott, O., & Olson, A. J. (2010). AutoDock Vina: Improving the speed and accuracy of docking with a new scoring function, efficient optimization, and multithreading. *Journal of Computational Chemistry, 31*(2), 455–461. https://doi.org/10.1002/jcc.21334

Yin, W., Mao, C., Luan, X., Shen, D.-D., Shen, Q., Su, H., Wang, X., Zhou, F., Zhao, W., Gao, M., Chang, S., Xie, Y.-C., Tian, G., Jiang, H.-W., Tao, S.-C., Shen, J., Jiang, Y., Jiang, H., Xu, Y., … Xu, H. E. (2020). Structural basis for inhibition of the RNA-dependent RNA polymerase from SARS-CoV-2 by remdesivir. *Science, 368*(6498), 1499–1504. https://doi.org/10.1126/science.abc1560

Publisher's Note & Disclaimer

All statements, opinions, and data in this publication were solely the responsibility of the individual authors or contributors and did not necessarily reflect the views of the publisher or editors. The publisher and editors did not guarantee the accuracy, completeness, or reliability of the content, and were not legally responsible for any errors, omissions, or consequences arising from its use. The publisher and editors also disclaimed any liability for injury, damage, or loss to persons or property resulting from the application of ideas, methods, or products mentioned herein. Readers were advised to independently verify all information before relying on it. The publisher accepted no responsibility for any consequences arising from the use of this publication's materials.

Supplementary Materials

Table S1. Phytochemical compounds reported in *Anacardium occidentale* leaves compiled from literature.

No.	Compound Name	References
1	2-Methylpentanoic acid	Awakan et al., 2018
2	Butanamide	Awakan et al., 2018
3	Hexanamide	Awakan et al., 2018
4	Agathisflavone	Chan et al., 2017
5	Amentoflavone	Chan et al., 2017
6	Chlorogenic acid	Chan et al., 2017
7	Kaempferol-3-O-arabinofuranoside	Chan et al., 2017
8	Kaempferol-3-O-glucoside	Chan et al., 2017
9	Myricetin	Chan et al., 2017
10	Peonidin	Chan et al., 2017
11	Quercetin	Chan et al., 2017
12	Quercetin-3-O-galactoside	Chan et al., 2017
13	Quercetin-3-O-glucoside	Chan et al., 2017
14	Quercetin-3-O-rhamnoside	Chan et al., 2017
15	Quercetin-3-O-rutinoside	Chan et al., 2017
16	Catechin	Khaleghi et al., 2011
17	Epicatechin	Khaleghi et al., 2011
18	Kaempferol	Khaleghi et al., 2011
19	Catechin-5-O-gallate	Sae-leaw & Benjakul, 2019
20	Epifisetinidiol-4alpha-OI	Sae-leaw & Benjakul, 2019
21	Epigallocatechin-7-O-gallate	Sae-leaw & Benjakul, 2019
22	Fisetin-8-C-glucoside	Sae-leaw & Benjakul, 2019
23	Gallocatechin	Sae-leaw & Benjakul, 2019
24	Hinokiflavone	Sae-leaw & Benjakul, 2019
25	Quercetin 3′-xyloside	Sae-leaw & Benjakul, 2019
26	Quercetin 3-(2″-galloyl-α-L-arabinopyranoside)	Sae-leaw & Benjakul, 2019
27	Quercetin-4-O-glucoside	Sae-leaw & Benjakul, 2019
28	Orientin-2″-O-gallate	Sae-leaw & Benjakul, 2019
29	Anthocyanidin	Schulze-Kaysers et al., 2015
30	Epicatechin-3-gallate	Załuski et al., 2015

References for Supplementary Table

Awakan, O. J., Malomo, S. O., Adejare, A. A., Igunnu, A., Atolani, O., Adebayo, A. H., & Owoyele, B. V. (2018). Anti-inflammatory and bronchodilatory constituents of leaf extracts of *Anacardium occidentale* L. in animal models. *Journal of Integrative Medicine, 16*(1), 62–70. https://doi.org/10.1016/j.joim.2017.12.009

Chan, E. W. C., Baba, S., Chan, H. T., Kainuma, M., Inoue, T., & Wong, S. K. (2017). Ulam herbs: A review on the medicinal properties of *Anacardium occidentale* and *Barringtonia racemosa*. *Journal of Applied Pharmaceutical Science, 7*(2), 241–247. https://doi.org/10.7324/JAPS.2017.70235

Khaleghi, S., Aziz, A. A., Razali, N., & Junit, S. M. (2011). Microarray analysis revealed different gene expression patterns in HepG2 cells treated with low and high concentrations of the extracts of *Anacardium occidentale* shoots. *Genes & Nutrition, 6*(4), 413–427. https://doi.org/10.1007/s12263-011-0216-z

Sae-leaw, T., & Benjakul, S. (2019). Prevention of quality loss and melanosis of Pacific white shrimp by cashew leaf extracts. *Food Control, 95*, 257–266. https://doi.org/10.1016/j.foodcont.2018.08.014

Schulze-Kaysers, N., Feuereisen, M. M., & Schieber, A. (2015). Phenolic compounds in edible species of the Anacardiaceae family - a review. *RSC Advances, 5*(89), 73301–73314. https://doi.org/10.1039/C5RA11746A

Załuski, D., Cieśla, Ł., & Janeczko, Z. (2015). The structure–activity relationships of plant secondary metabolites with antimicrobial, free radical scavenging and inhibitory activity toward selected enzymes. In A. Rahman (Ed.), *Studies in natural products chemistry* (Vol. 45, pp. 217–249). Elsevier. https://doi.org/10.1016/B978-0-444-63473-3.00007-1